Earthquake Science
地震学报英文版 ISSN 1674-4519 CN 11-5695/P

Determination of rupture directivity of the 2024 feidong *M*4.7 earthquake using single near-source station

Suli Yao, Zhigao Yang, Hongfeng Yang

Citation: Yao SL, Yang ZG, Yang HF (2025). Determination of rupture directivity of the 2024 feidong 4.7 earthquake using single near-source station. *Earthquake Science*, **38**(0): 1–9, doi:

View online:

Earthquake Science 38 (2025) 1–9

Contents lists available at ScienceDirect

Earthquake Science

Journal homepage: https://www.keaipublishing.com/en/journals/earthquake-science/

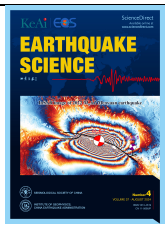

Determination of rupture directivity of the 2024 feidong *M*4.7 earthquake using single near-source station

Suli Yao[1,2], Zhigao Yang[3] and Hongfeng Yang[1,4,✉]

[1] *Department of Earth and Environmental Sciences*, *The Chinese University of Hong Kong*, *Hong Kong*, *China*
[2] *Department of Earth and Space Sciences*, *Southern University of Science and Technology*, *Shenzhen*, *China*
[3] *The China Earthquake Networks Center* (*CENC*), *Beijing*, *China]*
[4] *Shenzhen Research Institute*, *The Chinese University of Hong Kong*, *Shenzhen*, *China*

Key points:

- The 2024 *M*4.7 Feidong earthquake was well recorded by a 4-km-away strong-motion station;
- The S motion rotation at the near-source station reveals rupture propagation towards southwest;
- The inference of rupture propagation is further validated through comparing with M3 events in the sequence;
- Our study highlights the superior application or near-source observations in studying earthquake sources.

A B S T R A C T

Determining the rupture directivity for small earthquakes is challenging due to the small source dimension and limited resolution of far-field observations. In recent years, the burst of near-source observations provides great opportunities to study earthquake rupture. Here we present the rapid determination of the rupture directivity for the 2024 Feidong *M*4.7 earthquake using only one strong motion station located 4 km from the epicenter. We find that the polarization of S waves evolves during the rupture, indicating an azimuth change during the rupture propagation. Through comparing the data with the synthetic waveforms, we infer that the *M*4.7 event propagated dominantly to the southwest on the dextral Tanlu fault. Our inference is further validated through comparing the data with records at local stations for M3 earthquakes in the Feidong sequence. Our study highlights the superior application of near-source observations in earthquake source studies.

Keywords: 2024 *M*4.7 Feidong earthquake; near-source station; S polarization; rupture directivity

Citation: Yao SL, Yang ZG and Yang HF (2025). Determination of rupture directivity of the 2024 feidong *M*4.7 earthquake using single near-source station. Earthq Sci **38**, doi:

Production and Hosting by Elsevier on behalf of KeAI

Peer review under the responsibility of Institute of Geophysics, China Earthquake Administration.

✉ **Corresponding author.** Yang HF, email: hyang@cuhk.edu

Article history:

https://doi.org/

1. Introduction:

Resolving rupture process for small earthquakes (M<5) is a challenging task in seismology because of their rather small rupture areas. Commonly, small earthquakes are studied as point sources or by assuming simple symmetric source models, such as the circular rupture model introduced in *Brune (1970)* and the *Madariaga (1986)*. Small earthquakes feature short source durations and small rupture extents. Therefore, the information of rupture details is contained in relatively high-frequency signals that are generally affected by the path and site effects in seismograms at distance. Current studies on the rupture propagation of small earthquakes are mostly based seismic network, as the asymmetric ruptures can cause azimuth-dependent observations. For instance, some studies resolved rupture directivity by exploring the dependence of source spectra (e.g. Kane et al., 2013) and ground motion intensity (e.g. Boatwright, 2007) on azimuth, or used smaller events as empirical Greens' functions (EGFs) to obtain the apparent source time functions and identify rupture directivity (e.g. McGuire, 2004; Meng et al., 2020; Chen et al., 2021). Those studies revealed ubiquitous complexities of small earthquakes.

Except network-based approaches, single stations located very close to the earthquake sources can capture the rupture process in detail and thus are anticipated to provide constraints on rupture propagation (Fig. 1). In large earthquakes, the near-fault stations can record large velocity pulses when the rupture passes by, so called the rupture phases, as demonstrated in the 2023 M_W7.8 Kahramanmaraş, Tuŕkiye earthquake (Yao and Yang, 2025; Ren et al., 2024). The pulses contain the information of the local rupture time and slip-stress evolution on faults (Fukuyama and Mikumo, 2007; Chen et al., 2021). For small earthquakes, single-neat-source-station analysis was firstly applied by *Kanamori et al. (1990)* on a station located 4 km from the 1988 M_L 4.9 Pasadena earthquake to determine location, origin time, moment magnitude, and focal mechanism. Later the method was found to be efficient for small to moderate events (e.g. Singh et al., 1997; Pacheco and Singh, 1997) but the cases of applications are very limited in the past two decades because the fast development of station networks that can support more routine and rapid measurements. In addition, previous single-station studies have commonly ignored the spatial propagation of the rupture but only consider a fixed location and finite source time functions.

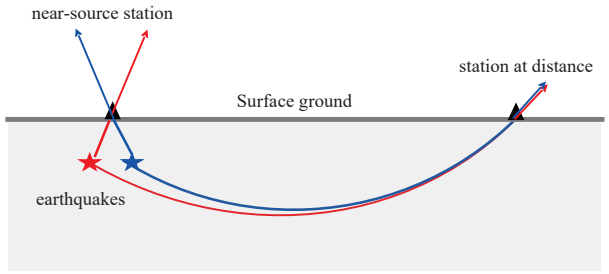

Figure 1. A schematic plot showing ray paths from earthquakes to a near-source station and to a station at distance. The arrows denote the incident angles.

Due to the short distance, the ray path to the near-source station may evolve even with limited rupture propagation length (Fig. 1). Therefore, the near-source stations have the great potential to resolve rupture process of small earthquakes. In this study, we explore extracting the rupture propagation directivity for the 2024 Feidong M4.7 earthquake using one strong-motion station that is located 4.4 km from the epicenter.

2. The 2024 Feidong M4.7 earthquake and near-source station A0006

On 18 Sep 2024, a M4.7 earthquake stuck Feidong County, Hefei, province, China. According to the China Earthquake Networks Center (CENC), this event occurred at coordinates 31.98°N,117.60°E at a depth of 10 km, near the boundary between the Yantze Plate and the North China Craton (Fig. 2a), and at the junction of the dextral Tanlu fault system and the reverse Feizhong fault (Fig. 2b). This event was preceded by a foreshock sequence with several M3 events including a M3.9 earthquake on 14 Sep 2024. Two M3 aftershocks occurred on 25 Sep (M3.8) and 01 Oct (M3.3). According to the right-lateral strike-slip focal mechanism (Yang et al., 2024; Ni et al., 2025), the M4.7 likely occurred on the Tanlu fault or a secondary fault in its vicinity (Li et al., 2016) (Fig. 2b).

The Feidong sequence was well recorded by the local strong motion stations (Fig.2a). The closest station is A0006, which located 4.4 km west of the mainshock (azimuth ~ 270°) (Fig. 2b). The coseismic ground motion during the M4.7 mainshock at station A0006 is very intense with a peak acceleration of 577 gal and a peak velocity of 28.3 cm/s in the EW component (Fig. 2a, 3a, & 3e). Given the event depth of ~10 km and the short epicentral distance, the incident angles of waves are small (Fig. 1) (~20°). Therefore, the P motions are nearly vertical, and S motions are dominantly horizontal (Fig. 3a & 3e). The time difference between P and S arrivals is ~1.5 second, consistent with the hypocentral distance of ~11 km (assume V_P = 5.1 km/s, V_S = 3.0 km/s).

Due to the short hypocentral distance of station A0006, the waveforms are dominated by large pulses related to the

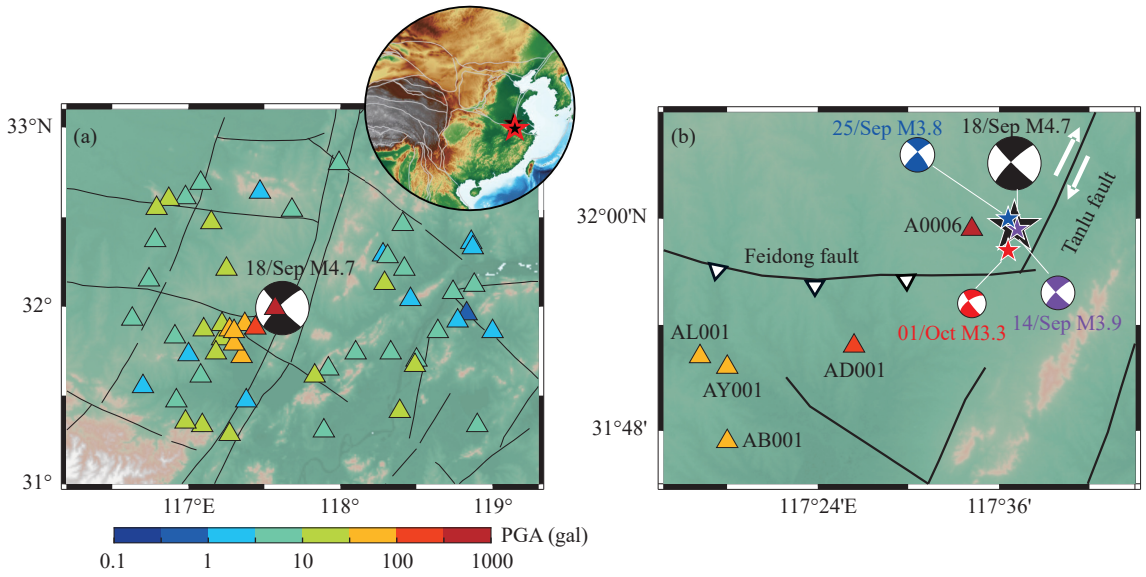

Figure 2. The map view for the 2024 Feidong earthquake sequence. (a) The distribution of peak ground accelerations (PGA) recorded by strong motion stations. The black beach ball represents the focal mechanism of the *M*4.7 event. The black lines are regional fault traces. (b) The zoom-in map plot for the *M*4.7 event and M3 events in this sequence. The triangles denote the strong motion stations within 40 km used in particle motion analysis.

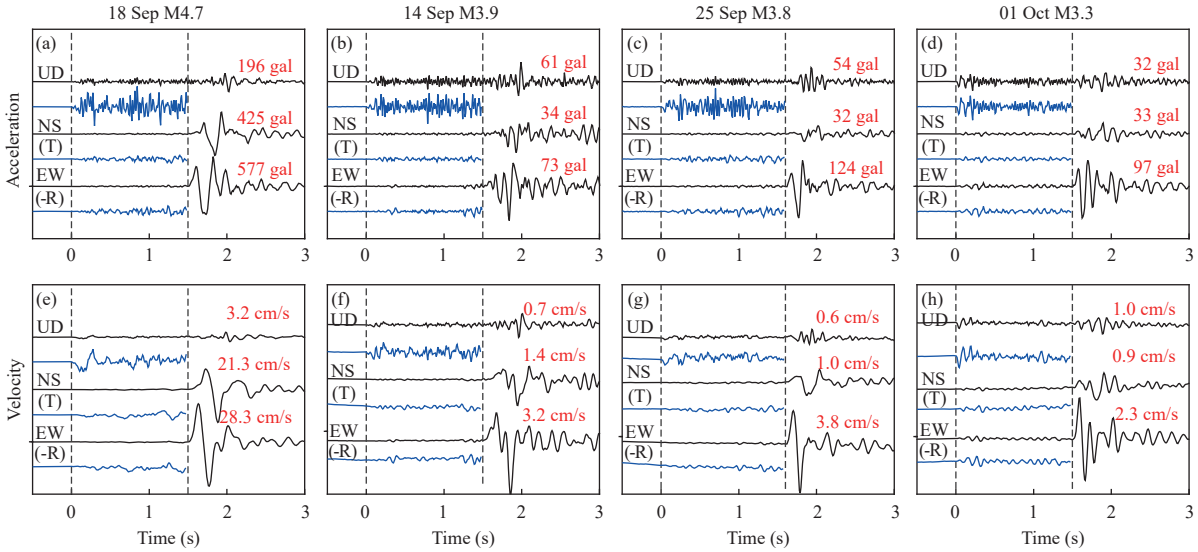

Figure 3. The three-component acceleration and velocity waveforms at station A0006 for the *M*4.7 (a & e) and three M3 events (b-d & f-h). The peak value of each trace is written aside in red. The two dashed lines mark the arrivals of P and S waves, respectively. The waveforms in blue provide the zoomed-in view for waves before S arrivals.

source. The P and S velocity pulses can be clearly identified with a duration of ~0.4 second (Fig. 3e), which likely corresponds to the source duration. Our following analysis will focus on the pulses at station A0006.

3. S motion reveals rupture propagation

The coseismic particle motion on the ground is controlled by the earthquake source focal mechanism and the receiver's relative location to the source. When the receiver is sufficiently close, the propagation of the rupture front-essentially the movement of the radiation source-can lead to significant changes in the relative location (azimuth) and, consequently, the particle motion at the receiver. Therefore, the ground particle motion can provide valuable insights into the source spatial migration. In this section, we will analyze the particle motion at station A0006 to infer the rupture directivity of the *M*4.7 main-shock. Considering the baseline shift and the small amp-

litudes of the P phase in the two horizontal components, the P polarization analysis may bare large uncertainties. Therefore, we focus on the S motion with large amplitudes.

We observe large S pulses in both EW and NS components. At the onset, the amplitude of EW pulse is much larger than NS (Fig. 4a) so that the motion is dominantly to the east (the phase I to II) (Fig. 4b). In the next stage, the EW motion reverses to westward while the NS motion remains to the north (II to III). In the last stage (III to IV), the motion is dominantly towards south.

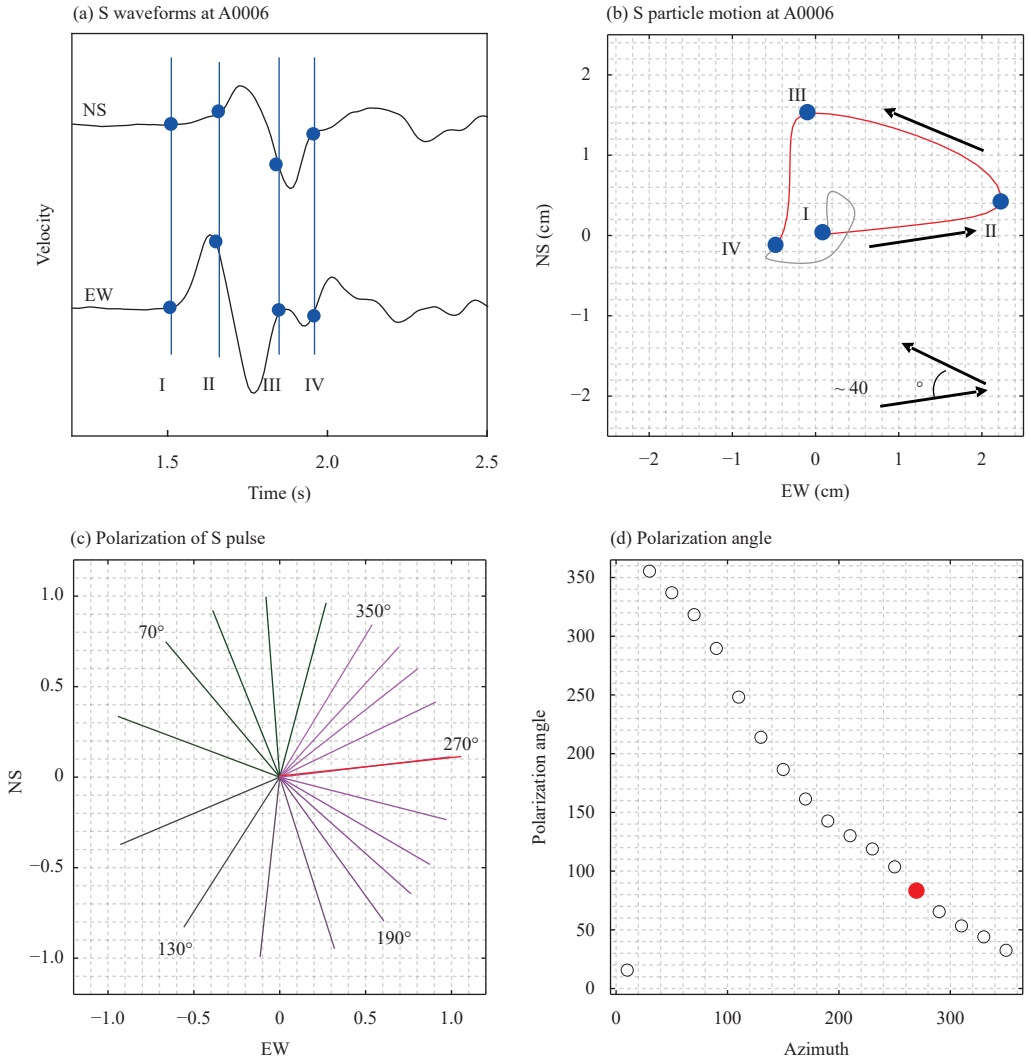

Figure 4. (a) S velocity pulses in NS and EW components at A0006. The blue dashed lines and dots marked four timings I-IV. (b) The S displacement particle motion at A0006. The four timings are marked as blue dots. The arrows indicate the major motion directions. (c) The synthetic S motion directions at different azimuths. The red line marks the S motion direction (polarization) at the azimuth of 270°, the azimuth of station A0006 to the hypocenter. (d) The S polarization angle versus azimuth. The red dot marks the polarization at the azimuth of 270°.

To understand the S motion rotation, we first investigate the synthetic S polarization for a point source. We model a point source in the half-space medium (V_S= 3.0 km/s and V_P=5.1 km/s). The focal mechanism and depth of the point source are prescribed according to the report of CENC (strike 226°, dip 80°, rake −175°, and depth 10 km). The epicentral distance is set to be 4 km. Then we use frequency-wavenumber (FK) integration method (Zhu and Rivera, 2002) to synthesize the Green's functions and the waveforms at various azimuths. After that, we plot the S motion using the synthetic waveforms. As shown in figure 4c and 4d, the S polarization changes with the azimuth of the receiver. The observed first S motion at A0006 is nearly toward east, which aligns with the prediction at the azimuth of 270°. The consistency supports the reliability of the reported hypocenter location and the focal mechanism. However, the single-point-source scenarios cannot explain the polarization rotation

(~40°) observed.

Here we propose the S rotation to be associated with earthquake rupture propagation. Considering the rotation direction and the synthetic polarization (Fig. 4c & 4d), the rupture is inferred to propagate to the southwest (Fig. 5a) along the local strike of 226°. We use simplified two-point-source model to demonstrate the rotation in figure 5. The hypocenter is positioned at an azimuth of 270° (AZ1). The southward rupture propagation leads to an increase of the azimuth from the source to A0006 (AZ2 > AZ1) (Fig. 5a). Along with the azimuth change, the synthetic NS motion gets enhanced related to the EW motion (Fig. 5c-5e), leading to the motion rotation (Fig. 5b). Notably, the model here is to demonstrate how the rotation occurs with the radiator moving to the south, while we do not intend to quantify any subevents in the mainshock.

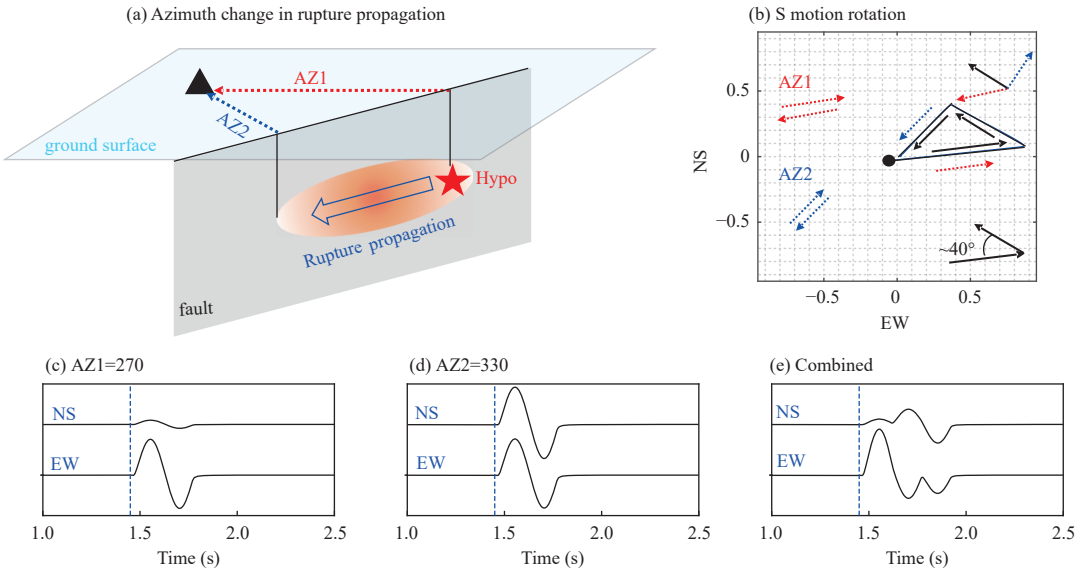

Figure 5. (a) A schematic plot showing the propagation of the rupture on the fault and the evolution of the azimuth of the receiving station A0006 on the ground. (b) The synthetic S displacement motion for the two-point-source model according to the synthetic velocity waveforms in panel (e). The black arrows mark the motion direction at different stages. The dashed red and blue arrows mark the S polarization caused by the sources at azimuths of AZ1 and AZ2, respectively. (c-e) The synthetic S velocity waves in the two horizontal components at station A0006 caused by sources at azimuths of AZ1 and AZ2, respectively, and their combination with a 0.15s shift. The blue dashed lines mark the S arrivals.

4. Structural effects and comparison with M3 earthquakes

In addition to source, the motion rotation might be related to the structural effects. In the section 2, we assume a half-space media to predict the particle motion. Here we test the 1-D layered velocity model. We combine the local shallow sediment layers (Ni et al., 2025) with the Crust 1.0 model (https://igppweb.ucsd.edu/~gabi/crust1.html) (Fig. 6a). Its impact on particle motion is very limited as the predictions are nearly the same with the half-space model (Fig. 6b-6f). We further test the impact of anisotropy by considering different arrivals and durations for S pulses in NS and EW components (Fig. 7). We find that the anisotropy can change the initial motion direction (align with the component with higher speed) (Fig. 7a). Anisotropy ~5% can cause minor S motion rotation (< 20%) (Fig. 7a). With higher anisotropy, the polarization will become more linear as the pulses in two components are more separated in timing (Fig. 7a-7c). As shown in figure 3 and 4, we do not observe obvious shifts in S arrivals between different components and the initial S motion aligns well with the prediction based on the half-space model. Therefore, the influence of the anisotropy should be slight. We also test the anisotropic attenuation through prescribing different Q values (1 000, 400, and 100) for S waves in NS and EW components (Fig. 8). Given the short ray path, the influence of attenuation is quite minor (Fig. 8a). Despite above factors, other structural effects such as the topographic amplification may also contribute to the local particle motion.

To further validate that S motion rotation is not solely from the structure but contain the contribution of rupture propagation, we check the S motion for other three M3 events in the sequence, including the *M*3.9 foreshock on 14 Sep, the *M*3.8 aftershock on 25 Sep, and the *M*3.3 aftershock on 01 Oct (Fig. 3). According to the reports of

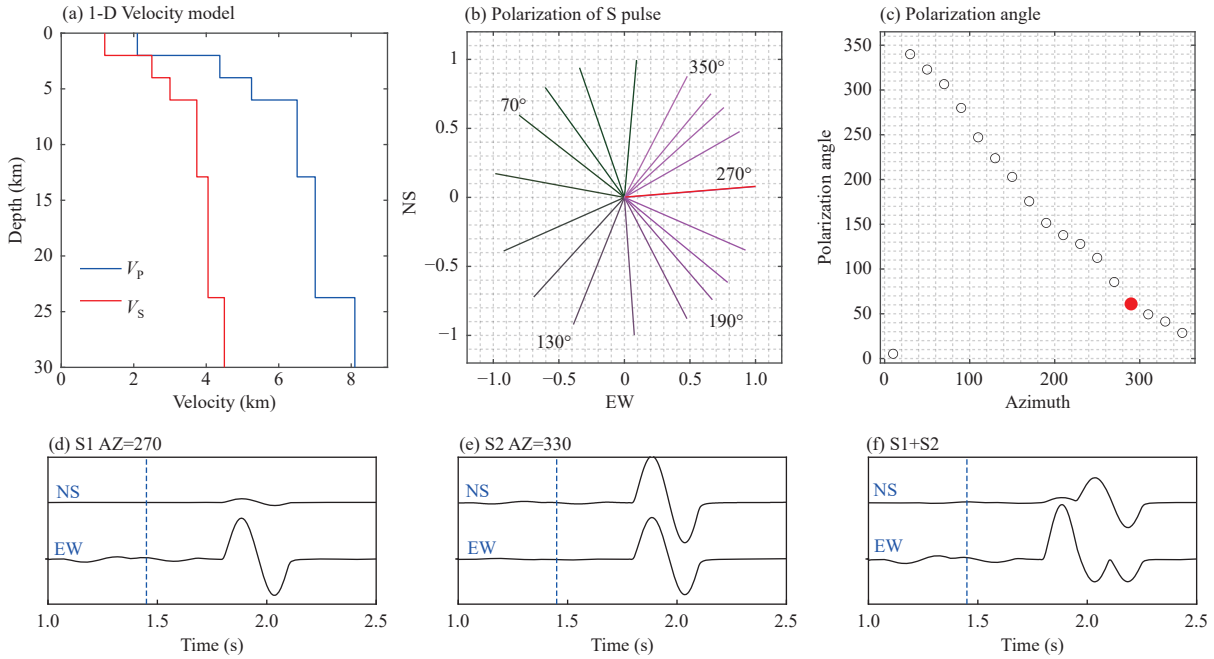

Figure 6. The synthetic test with 1-D layered velocity model. (a) The V_P and V_S versus depth in the layered model. (b) & (c) Same plots with figure 4c and 4d but based on the layered velocity model. (d)-(f) Same plots with figure 5c-5e but based on the layered velocity model.

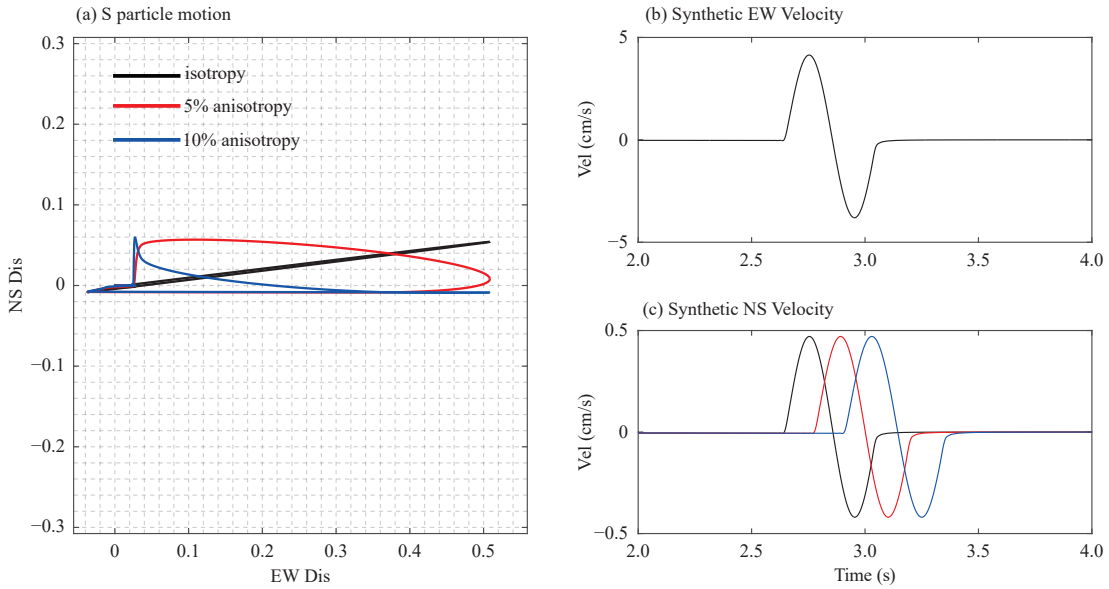

Figure 7. The synthetic test with anisotropy. (a) The predicted displacement particle motion with no anisotropy (black), 5% anisotropy (red), and 10% anisotropy (blue). (b) & (c) The synthetic EW and NS velocity waveforms. Here we decrease the velocity for SH component (NS) and keep the velocity for the SV waves constant to prescribe the anisotropy. The arrivals are shifted and the pulse widths are changed accordingly based on the anisotropy.

CENC and a recent study (Ni et al., 2025), the hypocenters of those events are very close with nearly identical focal mechanisms. Therefore, the effects of path and structure at local stations for the three events are nearly the same. Similar to the synthetics (Fig. 5c), the *M*3.8 event cause single S pulses in horizontal components with large EW-to-NS ratio (Fig. 3g), indicating a simple rupture process analog to the point-source scenario. While waveforms of the *M*3.9 and *M*3.3 events show more complexities likely associated with heterogeneous rupture process (Fig. 3f & 3h). Despite the waveform complexities, the ratio between peak velocities in NS and EW components (NS/EW) is

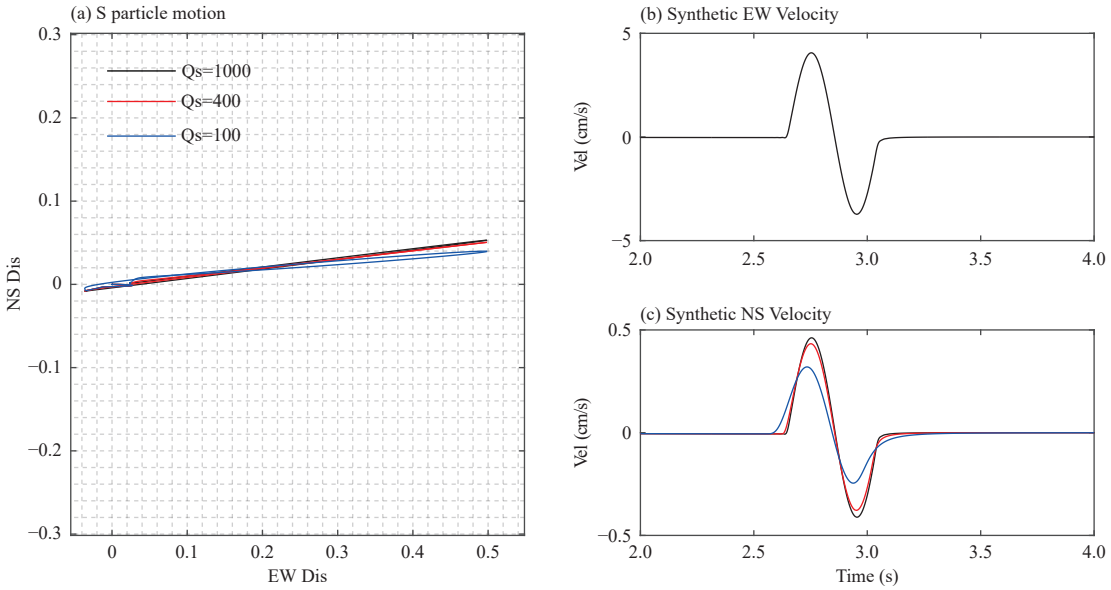

Figure 8. The synthetic test with different Q values. We keep the Q for the SV waves constant (i.e. 1 000) and change the Q for the SH waves (NS). (a) The predicted displacement particle motion with Q of 1 000 (black), 400 (red), and 100 (blue) for the SH waves, respectively. (b) & (c) The synthetic EW and NS velocity waveforms.

obviously higher in the mainshock compared to other three events. According to the synthetics (Fig. 4c & 4d, 5c-5e), the NS/EW ratio is small at the azimuth of 270° and increases as the source moves to southwest. Therefore, the higher NS/EW ratio is consistent the inference of directivity to the southwest in the *M*4.7 event.

We further compare the S particle motion of the *M*4.7 and the *M*3.8 event (Fig. 9) at local stations within 40 km (Fig. 2b). As the later event is an analog to the point-source scenario, the differences in particle motion should reflect different source processes in the two events. Stations with strong low-frequency noise are excluded in this analysis as no reliable particle motion can be extracted. The initial motion directions are nearly identical in the two events at all stations, proving the consistency in location and focal mechanism (Fig. 9). At A0006, the S motion in the M3.8 event also rotates but the rotation is much minor (i.e. 20°). Given limited rupture extent of a *M*3.8 event, the motion rotation in the aftershock is likely controlled by the local structure. Therefore, similar structural effect should also contribute to the motion during the mainshock. As the rotation in mainshock is obviously more significant compared to the aftershock, we propose that rupture propagation effect is needed to explain the observations in addition to the structural effects. At station AD001, the S motion of the mainshock is more complex compared to the aftershock (Fig. 9). The azimuth from the hypocenter to AD001 is 233°, nearly aligning with the fault strike of 226°. Therefore, the change of station azimuth caused by rupture propagation along the strike is negligible. The complexities in the mainshock motion may result from different arrivals of energy spikes radiated from asperities. With the increase of hypocentral distance, the resolution of the motion to the source process decreases and the structural effects dominate. So that the two events result in very similar S motion at stations AB001, AY001, and AL001 (Fig. 9).

The above analyses suggest that the motion rotation at station A0006 of the mainshock suggests the rupture directivity to the southwest. Given the truth that structure also contributes, we cannot directly quantify source parameters such as rupture speed and rupture extent from the rotation. To explore more detailed rupture process, thorough understanding on those structural factors is demanded.

5. Conclusion

In this study, we infer the rupture directivity of the 2024 *M*4.7 Feidong earthquake through analyzing the S particle motion at a near-source strong motion station. We identify a 40° rotation in the S polarization which can be explained by dominant rupture propagation to the southwest. Through analyzing structural effects and checking the data for other M3 events, we confirm that the 40° rotation is not a generic characteristic of the sequence controlled by the structure but is associated with the source process. Our study demonstrates the application of near-source stations in resolving rupture directivity of small earthquakes.

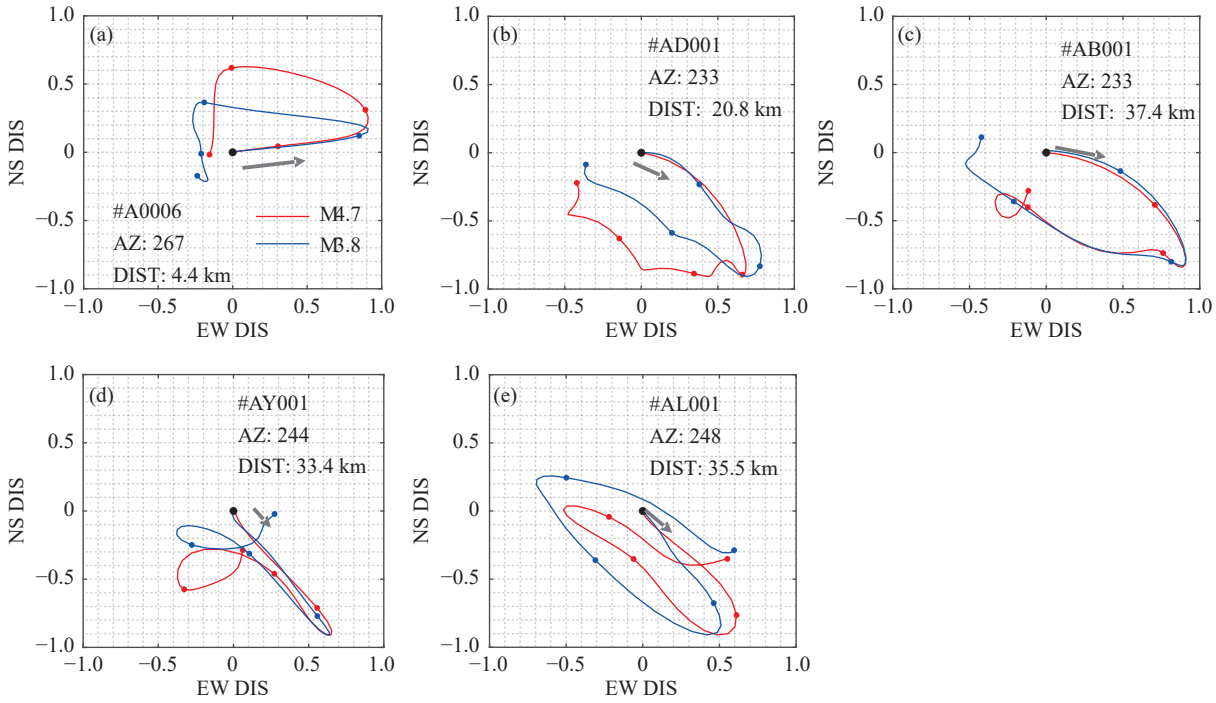

Figure 9. The displacement particle motion in the *M*4.7 (red) and *M*3.8 (blue) events at different strong motion stations. The distance and azimuth of each station to the hypocenter are written inside each panel. The dots mark the timings every 0.1 second. The amplitudes of the particle motions are normalized.

Acknowledgement:

S. Yao is partially supported by a Postdoc Fellowship from Faculty of Science, CUHK. H. Yang acknowledged the support from National Key R&D Program of China (2023YFF0803202) and HKSAR RGC (14308523). Z. Yang acknowledged the support from the Earthquake Spark Technology Project (XH23051B). This study benefited from the valuable discussion with Aqeel Abbas, Jiewen Zhang, Jinping Zi, and Junhao Song at the Chinese University of Hong Kong.

Conflict of interest

The authors affirm that they have no financial and personal relationships with any individuals or organization that could have potentially influenced the work presented in this paper.

References

Aki K (1993). Local site effects on weak and strong ground motion. Tectonophysics **218**(1-3): 93–111. https://doi.org/10.1016/0040-1951(93)90262-I.

Boatwright J (2007). The persistence of directivity in small earthquakes. Bull Seismol Soc Am **97**(6): 1850–1861. https://doi.org/10.1785/0120050228.

Brune JN (1970). Tectonic stress and the spectra of seismic shear waves from earthquakes. J Geophys Res **75**(26): 4997–5009. https://doi.org/10.1029/JB075i026p04997.

Chen H, He XH, Yang HF and Zhang JY (2021). Fault - plane determination of the 4 January 2020 offshore pearl river delta earthquake and its implication for seismic hazard assessment. Seismol Res Lett **92**(3): 1913–1925. https://doi.org/10.1785/0220200232.

Chen X, Yang HF and Jin MP (2021). Inferring critical slip - weakening distance from near - fault accelerogram of the 2014 M_W 6.2 Ludian earthquake. Seismol Res Lett **92**(6): 3416–3427. https://doi.org/10.1785/0220210089.

Fukuyama E and Mikumo T (2007). Slip-weakening distance estimated at near-fault stations. Geophys Res Lett **34**(9): L09302. https://doi.org/10.1029/2006GL029203.

Kanamori H, Mori J and Heaton TH (1990). The 3 December 1988, Pasadena earthquake (M_L = 4.9) recorded with the very broadband system in Pasadena. Bull Seismol Soc Am **80**(2): 483–487. https://doi.org/10.1785/BSSA0800020483.

Kane DL, Shearer PM, Goertz-Allmann BP and Vernon FL (2013). Rupture directivity of small earthquakes at Parkfield. J Geophys Res: Solid Earth **118**(1): 212–221. https://doi.org/10.1029/2012JB009675.

Li YC, Shan XJ, Song XG, Jiang Y, Gan WJ, Qu CY and Wang ZJ (2016). Fault locking and slip rate deficit on the middle and southern segment of the Tancheng-Lujiang fault inverted from GPS data. Chin J Geophys **59**(11): 4022–4034. https://doi.org/10.6038/cjg20161108 (in Chinese with English abstract).

Madariaga R (1976). Dynamics of an expanding circular fault. Bull Seismol Soc Am **66**(3): 639–666. https://doi.org/10.1785/BSSA0660030639.

McGuire JJ (2004). Estimating finite source properties of small earthquake ruptures. Bull Seismol Soc Am **94**(2): 377–393. https://doi.org/10.1785/0120030091.

Meng HR, McGuire JJ and Ben-Zion Y (2020). Semiautomated estimates of directivity and related source properties of small to moderate Southern California earthquakes using second seismic moments. J Geophys Res: Solid Earth **125**(4): e2019JB018566. https://doi.org/10.1029/2019JB018566.

Moczo P, Kristek J, Bard PY, Stripajová S, Hollender F, Chovanová Z, Kristeková M and Sicilia D (2018). Key structural parameters affecting earthquake ground motion in 2D and 3D sedimentary structures. Bull Earthq Eng **16**(6): 2421–2450. https://doi.org/10.1007/s10518-018-0345-5.

Ni HY, Li JL, Yao HJ, Huang XL, Li LL, Zhou DR, Wang XL, Yu SY, Lu YC, Yu JF, Zheng HG, Zhou GL, Zou HW, Yang W, Zhang M, Chen GY, Lin Y, Peng GL, Li ZF and Li HP (2025). Preliminary study of the tectonic structure and seismogenic environment of the *M*4.7 Feidong earthquake sequence on September 18, 2024 in Hefei. Earthq Sci **38**(3): 244–262. https://doi.org/10.1016/j.eqs.2024.11.001.

Pacheco JF and Singh SK (1998). Source parameters of two moderate Mexican earthquakes estimated from a single-station, near-source recording, and from MT inversion of regional data: a comparison of the results. Geofisica Int **37**(2): 95–102. https://doi.org/10.22201/igeof.00167169p.1998.37.2.398.

Ren CM, Wang ZX, Taymaz T, Hu N, Luo H, Zhao ZY, Yue H, Song XD, Shen ZK, Xu HY, Geng JH, Zhang W, Wang T, Ge ZX, Irmak TS, Erman C, Zhou YJ, Li Z, Xu H, Cao BN and Ding H (2024). Supershear triggering and cascading fault ruptures of the 2023 Kahramanmaraş, Türkiye, earthquake doublet. Science **383**(6680): 305–311. https://doi.org/10.1126/science.adi1519.

Singh SK, Pacheco J, Courboulex F and Novelo DA (1997). Source parameters of the Pinotepa Nacional, Mexico, earthquake of 27 March, 1996 (M_W = 5.4) estimated from near-field recordings of a single station. J Seismol **1**(1): 39–45. https://doi.org/10.1023/A:1009741712512.

Yang ZG, Xu TR and Liang JH (2024). Towards fast focal mechanism inversion of shallow crustal earthquakes in the Chinese mainland. Earthq Res Adv **4**(2): 100273. https://doi.org/10.1016/j.eqrea.2023.100273.

Yao SL and Yang HF (2025). Rupture phases reveal geometry-related rupture propagation in a natural earthquake. Sci Adv **11**(4): eadq0154. https://doi.org/10.1126/sciadv.adq0154.

Zhu LP and Rivera LA (2002). A note on the dynamic and static displacements from a point source in multilayered media. Geophys J Int **148**(3): 619–627. https://doi.org/10.1046/j.1365-246X.2002.01610.x.